Topological and magnetic phases with strong spin-orbit coupling on the hyperhoneycomb lattice

Eric Kin-Ho Lee,[1] Subhro Bhattacharjee,[1,2] Kyusung Hwang,[1] Heung-Sik Kim,[3] Hosub Jin,[4,5] and Yong Baek Kim[1,6]

[1]*Department of Physics and Center for Quantum Materials, University of Toronto, Toronto, Ontario, Canada M5S 1A7*

[2]*Max-Planck-Institut für Physik komplexer Systeme, Nöthnitzer Str. 38, 01187 Dresden, Germany*

[3]*Department of Physics, Korean Advanced Institute of Science and Technology, Daejun 305-701, Korea*

[4]*Center for Correlated Electron Systems, Institute for Basic Science (IBS), Seoul 151-747, Korea*

[5]*Department of Physics and Astronomy, Seoul National University, Seoul 151-747, Korea*

[6]*School of Physics, Korea Institute for Advanced Study, Seoul 130-722, Korea*

(Received 18 March 2014; published 28 May 2014)

We study the general phase diagram of correlated electrons for iridium-based (Ir) compounds on the hyperhoneycomb lattice, a crystal structure where the Ir^{4+} ions form a three-dimensional network with threefold coordination recently realized in the β-Li_2IrO_3 compound. Using a combination of microscopic derivations, symmetry analysis, and density functional calculations, we determine the general model for the electrons occupying the $j_{\text{eff}} = \frac{1}{2}$ orbitals at the Ir^{4+} sites. In the noninteracting limit, we find that this model allows for both topological and trivial electronic band insulators along with metallic states. The effect of Hubbard-type electron-electron repulsion on the above electronic structure in stabilizing $\mathbf{q} = \mathbf{0}$ magnetic order reveals a phase diagram with continuous phase transition between a topological band insulator and a Néel ordered magnetic insulator.

DOI: 10.1103/PhysRevB.89.205132 PACS number(s): 71.15.Mb, 75.10.Lp, 71.70.Ej, 03.65.Vf

I. INTRODUCTION

The importance of the interplay between spin-orbit coupling (SOC) and electron-electron correlations in stabilizing a wide variety of novel electronic phases such as topological insulators (TI), Weyl semimetals, and quantum spin liquids has been explored recently [1–7]. Materials such as 5*d* transition-metal (iridium = Ir, osmium = Os) oxides with strong atomic SOC provide fertile grounds to uncover the above physics and a large number of such compounds are currently being investigated [8–16].

Recently, the material β-Li_2IrO_3 has been synthesized by Takayama *et al.* [17] which has attracted attention due to the novel three-dimensional network formed by the Ir^{4+} ions: the hyperhoneycomb lattice (see Fig. 1). It has been theoretically predicted that the spin model in the strong-coupling limit can be highly anisotropic and may lead to interesting magnetic as well as a three-dimensional Kitaev quantum spin-liquid ground state [18–21].

In this paper, motivated by the above developments, we study the weak- and intermediate-coupling regimes of β-Li_2IrO_3 and isostructural compounds with Ir situated on a hyperhoneycomb lattice. We point out the possibility of interesting ground states in these systems that generally arise from the nature of the underlying lattice geometry and strong SOC effects. In turn, these results can shed light on the physics of the above material and others on a similar lattice structure.

An important starting point in the study of these compounds is to ascertain the nature of the electronic structure, particularly that of the electronic bands near the Fermi level. Due to the large atomic SOC, as in a large number of Ir-based compounds [3,6,12,13,22,23], the low-energy bands are expected to be formed by $j_{\text{eff}} = \frac{1}{2}$ atomic orbitals. Using the symmetries of the hyperhoneycomb lattice, we obtain the general tight-binding Hamiltonian for the $j_{\text{eff}} = \frac{1}{2}$ orbitals. Apart from the generic metal and band insulator (BI), we find that this hopping Hamiltonian allows for a three-dimensional strong TI (STI) over a large parameter regime. The above tight-binding model is further justified by more microscopic calculations based on Slater-Koster parameters for the 5*d* orbitals in the large SOC limit for the *ideal* hyperhoneycomb lattice. This latter calculation also reveals the connection between the symmetry-allowed hopping parameters and the Slater-Koster parameters. In parallel, we perform density functional theory (DFT) calculations in the presence of SOC to probe the nature of the states near the Fermi level for β-Li_2IrO_3 on an ideal hyperhoneycomb lattice. The DFT results support our assumption that the low-energy states near the Fermi level have a predominantly $j_{\text{eff}} = \frac{1}{2}$ orbital character and are well separated from the $j_{\text{eff}} = \frac{3}{2}$ bands that lie below the Fermi level. The study of the $\mathbf{q} = \mathbf{0}$ magnetic phases induced by Hubbard-type electronic correlations on the above electronic structure reveals an interesting phase diagram. We find a direct continuous transition between the STI at weak correlations and magnetic insulator with Néel order at intermediate correlations. Although the metallic state in the weak-coupling limit ultimately transitions into the Néel ordered magnetic insulator at sufficiently large correlations, an intermediate phase [a magnetically ordered (Néel) metal] is first reached via a discontinuous transition. Interestingly, while time-reversal and inversion symmetries are broken in the magnetically ordered insulator, the product of the two is found to be preserved, leading to pseudo-Kramers doublets in the energy spectrum.

The rest of the paper is organized as follows. We begin with a discussion of the ideal hyperhoneycomb lattice and its symmetries in Sec. II. Using these symmetries, the general tight-binding model (up to second-nearest neighbor, 2NN) for the $j_{\text{eff}} = \frac{1}{2}$ orbitals is then obtained in Sec. III. The hopping Hamiltonian contains both spin-conserving (scalar) as well as spin-flipping (vector) hopping amplitudes. While we show that the nearest-neighbor (1NN) vector hopping terms are inconsequential, the 2NN hopping terms can stabilize a three-dimensional STI over a large parameter regime. We study the detailed phase diagram of the symmetry-allowed tight-binding Hamiltonian in Sec. IV and point out a simple relation in the hopping parameters that separates the trivial and the topological band insulators in the phase diagram. In Sec. V,

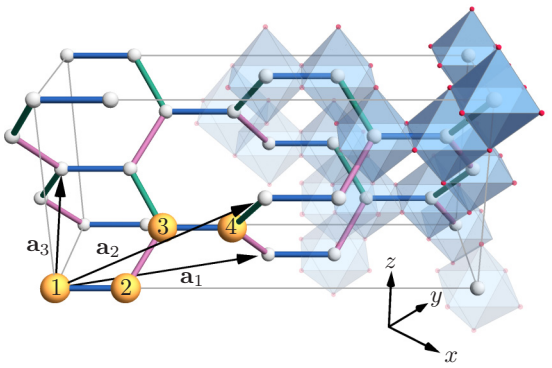

FIG. 1. (Color online) The ideal hyperhoneycomb lattice. The Ir^{4+} atoms (denoted by white spheres, except for the four yellow ones that indicate the four atoms in our unit cell) sit in octahedral cages (shaded in blue) of oxygen atoms (small red spheres). The lattice vectors are denoted by $\mathbf{a}_1$,$\mathbf{a}_2$, and $\mathbf{a}_3$. The three nearest-neighbor bonds are referred to as x (pink), y (green), and z (blue) bonds.

we establish the connection between the symmetry-allowed hopping parameters and the more microscopic Slater-Koster parameters characterizing the hopping Hamiltonian for the underlying t_{2g} bands. In this section, starting from such a hopping Hamiltonian on an ideal hyperhoneycomb lattice and taking the large SOC limit, we derive the pertinent Hamiltonian for the $j_{\rm eff} = \frac{1}{2}$ orbitals to the leading order of perturbation theory. In Sec. VI, we show the results of fully relativistic DFT calculations on β-Li_2IrO_3 assuming an ideal hyperhoneycomb lattice for the material. These calculations reveal the generic separation of the $j_{\rm eff} = \frac{1}{2}$ bands and the $j_{\rm eff} = \frac{3}{2}$ bands with the former being closer to the Fermi level, justifying our generic $j_{\rm eff} = \frac{1}{2}$ tight-binding calculations in earlier sections. Further, fitting the DFT band structure with the t_{2g} tight-binding model, we obtain an estimate of the parameter regime of the tight-binding model which may be relevant to β-Li_2IrO_3. After completing the characterization of the low-energy electronic structure, in Sec. VII, we study the effect of short-range electron-electron interactions in the intermediate correlation regime.

II. IDEAL HYPERHONEYCOMB LATTICE OF Ir^{4+} IONS

We first consider the generic symmetry-allowed $j_{\rm eff} = \frac{1}{2}$ tight-binding model for the network of Ir in the hyperhoneycomb lattice. As described in the following and also supported by our DFT calculations in Sec. VI, these $j_{\rm eff} = \frac{1}{2}$ orbitals are expected to form the low-energy electronic excitations near the Fermi level. To this end, we start with a description of the hyperhoneycomb lattice and its symmetries.

The hyperhoneycomb lattice consists of a network of Ir^{4+} ions where each Ir^{4+} ion has three 1NNs and sits in an octahedral oxygen cage (Fig. 1). A detailed structural description of the lattice can be obtained from the x-ray diffraction experiments on β-Na_2PtO_3 [24] which belongs to the same space group ($Fddd$) as β-Li_2IrO_3. In the ideal structure, which we refer in this paper as the *ideal* hyperhoneycomb lattice (shown in Fig. 1), the oxygen octahedra are undistorted and the Ir-O-Ir and the Ir-Ir-Ir bond angles measure 90° and 120°, respectively, and hence different Ir-Ir bonds have the same length.

The lattice structure can be described as a face-centered orthorhombic lattice with four Ir sites per unit cell [19]. While a complete discussion of the symmetries of the lattice is given in Ref. [19], here we note that since the hyperhoneycomb lattice possesses inversion symmetry, the eight bands arising from two $j_{\rm eff} = \frac{1}{2}$ orbitals at each of the four sublattices become four doubly degenerate bands due to Kramers theorem. In the following, we also exploit the presence of this inversion symmetry by using parity eigenvalues when computing the Z_2 topological invariants [25]. Out of the three 1NN bonds (which we call the x, y, and z, following notation used in the Heisenberg-Kitaev model explored in Refs. [19,20], see Fig. 1), two of the bonds (namely, x and y) are equivalent due to the presence of C_2 symmetry. More details regarding the lattice used in our ideal hyperhoneycomb calculations can be found in Appendix A.

At each Ir^{4+} site, the octahedral crystal field of the oxygen splits the $5d$ Ir orbitals into the upper e_g orbitals (fourfold degenerate including spin degeneracy) and the low-lying t_{2g} orbitals (sixfold degenerate including spin degeneracy) with the separation ($10Dq$) being approximately 3 eV. Neglecting the $t_{2g} - e_g$ mixing due to large energy separation, the strong SOC ($\lambda \sim 500$ meV) splits the six t_{2g} orbitals into the low-energy four $j_{\rm eff} = \frac{3}{2}$ quadruplet and high energy $j_{\rm eff} = \frac{1}{2}$ doublet. The five $5d$ electrons completely fill up the quadruplet leaving the doublet half-filled. These half-filled $j_{\rm eff} = \frac{1}{2}$ atomic orbitals, one at each Ir^{4+} site, form the low-energy electronic degrees of freedom in this compound.

A few remarks are in order before we proceed to the description of the tight-binding and DFT results. While the symmetry-allowed tight-binding model described in Sec. III is generally valid for changes in the position of both oxygen and the Ir^{4+} ions as long as the space group ($Fddd$) remains intact and the $j_{\rm eff} = \frac{1}{2}$ bands remain well separated from the $j_{\rm eff} = \frac{3}{2}$ bands, the microscopic calculations starting from the t_{2g} orbitals presented in Sec. V assume ideal position of the oxygen atoms which in turn affect the overlap integrals. The effective hopping Hamiltonian for the $j_{\rm eff} = \frac{1}{2}$ derived from it assumes that the the leading-order corrections due to SOC coupling effects are captured within a second-order perturbation theory which is valid in the large SOC limit. Since the detailed structure of β-Li_2IrO_3 is not available at present and also future compounds may differ by small details in the structure such as the position of oxygen ions, we start with the most general case in Sec. III and specialize to the ideal hyperhoneycomb lattice later. Our DFT calculations in Sec. VI, based on the ideal structure for β-Li_2IrO_3, validate our above assumption of the separation of the $j_{\rm eff} = \frac{1}{2}$ and $j_{\rm eff} = \frac{3}{2}$ bands in that limit.

III. SYMMETRY-ALLOWED TIGHT-BINDING MODEL

Using various symmetries of the lattice discussed above, we can write the generic tight-binding model for the $j_{\rm eff} = \frac{1}{2}$ electrons on the hyperhoneycomb lattice. The general hopping Hamiltonian is given by

$$H_{\rm tb} = \sum_{ij} c_i^\dagger h_{ij} c_j \qquad (1)$$

with

$$h_{ij} = t_{ij}\mathbb{I} + i\mathbf{v}_{ij}\cdot\sigma, \tag{2}$$

where $c_i^\dagger = (c_{i\uparrow}^\dagger, c_{i\downarrow}^\dagger)$ are the creation operators in the $j_{\text{eff}} = \frac{1}{2}$ basis at site i, $\vec{\sigma} = (\sigma_x,\sigma_y,\sigma_z)$ are the Pauli matrices, and $\mathbb{I}$ is the 2×2 identity matrix. t_{ij} and $\mathbf{v}_{ij}$ denote the scalar and the spin-flip hopping, respectively [26].

In the following, we determine the hopping Hamiltonian up to second-nearest neighbor (2NN). A more microscopic approach based on Slater-Koster parameters including various hopping paths and its connection to the symmetry-allowed hopping parameters is presented in Sec. V.

A. Nearest neighbor

At the nearest-neighbor level (1NN), as noted earlier, there are two symmetry-inequivalent sets of bonds to consider: the x/y bonds and the z bonds. The symmetry-allowed 1NN tight-binding hopping matrix Eq. (2) can be written as

$$h_{x/y}^{1\text{NN}} = t_{xy}\mathbb{I} \tag{3}$$

for the x/y bonds and

$$h_z^{1\text{NN}} = t_z^{1\text{NN}}\mathbb{I} + i\mathbf{v}_z^{1\text{NN}}\cdot\sigma \tag{4}$$

for the z bonds. The absence of spin-dependent vector hopping amplitudes on the x and y bonds is due to inversion symmetry at their bond centers. Each z bond, on the other hand, has three C_2 axes passing through its bond center, which constrains the spin-dependent vector hopping amplitudes to point in the $\pm(\hat{x}+\hat{y})$ direction. We use the convention $\hat{v}_z^{(12)} = (1,1,0)/\sqrt{2}$ and, by symmetry, $\hat{v}_z^{(34)} = -(1,1,0)/\sqrt{2}$, where the superscripts indicate sublattice indices that are involved in the particular z bond.

We note that in the purely 1NN model, the spin-dependent vector hopping amplitude on the z bonds can be eliminated by a sublattice-dependent basis transformation. To see this, we rewrite the z-bond hopping amplitudes (4) as

$$h_z^{1\text{NN}} = \sqrt{\left(t_z^{1\text{NN}}\right)^2 + \left|\mathbf{v}_z^{1\text{NN}}\right|^2}\, e^{i\theta\hat{v}_{ij}\cdot\vec{\sigma}}, \tag{5}$$

where, $\tan\theta = |\mathbf{v}_z^{1\text{NN}}|/t_z^{1\text{NN}}$. Rotating the $j_{\text{eff}} = \frac{1}{2}$ electrons on sublattices 2 and 3, for example, by $\exp(-i\theta\hat{v}_z\cdot\vec{\sigma})$ would render hopping amplitudes on the z bonds diagonal in $j_{\text{eff}} = \frac{1}{2}$ pseudospin space without affecting the form of the hopping on the x and y bonds which are already diagonal in the pseudospin indices.

In other words, the generic symmetry-allowed 1NN $j_{\text{eff}} = \frac{1}{2}$ tight-binding model on the hyperhoneycomb can always be written in an SU(2)-invariant form (in pseudospin space) with the appropriate choice of basis. Immediately, we conclude that the generic band structure is particle-hole symmetric because the model is bipartite (see end of Sec. III B and Appendix C for general discussion on particle-hole symmetry). In addition, all band insulators obtained from this 1NN model would be topologically trivial and a topologically nontrivial band insulator *can not* be realized with 1NN bonds alone. This is shown in the phase diagram (Fig. 2) of the 1NN tight-binding model at half-filling as a function of t_{xy}/t_z.[1] The phase diagram contains a trivial band insulator and a metal. In the limit where $t_{xy} = 0$, the hyperhoneycomb lattice reduces to independent dimers which is a topologically trivial insulating state with flat bands. For $0 < 2t_{xy} < t_z$, the flat bands disperse but the band structure remains gapped. At $2t_{xy} = t_z$, band touching occurs at the Γ point. The dispersion along the Γ-Z direction is linear near the band touching, while it is quadratic in the Γ-X and Γ-Y directions. As t_{xy} increases such that $2t_{xy} > t_z$, the band touching moves away from the Γ point and the Fermi surface becomes a closed line node in the Γ-X-A_1-Y plane of the Brillouin zone. This is an interesting feature of the strictly 1NN model that the metal has a one-dimensional Fermi surface, i.e., a closed Fermi line node, instead of a regular two-dimensional Fermi surface. Despite having a line node away from the time-reversal-invariant momenta (TRIM) points, this semimetallic phase is proximal to a STI in the following sense: if we blindly computed the Z_2 topological indices using the parity eigenvalues of the occupied bands, it would result in the indices (1;000). Since the line node is not protected by symmetries, introducing additional hopping amplitudes may gap out the entire line node and thus generate a STI. In Sec. III B, we will show that certain 2NN hopping amplitudes serve this precise role and hence a STI can be realized on the hyperhoneycomb lattice.

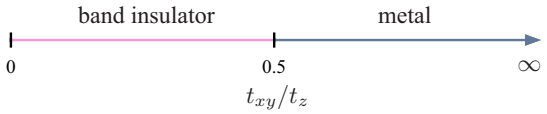

FIG. 2. (Color online) Phase diagram for the strictly nearest-neighbor hopping Hamiltonian. The band insulator is topologically trivial and the metal has a closed one-dimensional line node forming the Fermi surface.

As described in Sec. V, starting with the t_{2g} hopping Hamiltonian on the ideal hyperhoneycomb lattice and taking the strong SOC limit, we find that, to the lowest order, the resulting effective $j_{\text{eff}} = \frac{1}{2}$ model is described by $t_{xy} = t_z$ and $\theta = 0$. This falls in the metallic regime in the phase diagram shown in Fig. 2. Here, we point out that when distortions are accounted for and/or higher-order terms are included in the perturbative series, t_{xy} and t_z would be in general different and θ may be finite.

B. Second-nearest neighbor

For the 2NN hopping, both the scalar and spin-dependent hopping terms are generally nonzero. There are 20 2NN bonds in the hyperhoneycomb lattice when using the primitive unit cell (see Appendix B for details). These 20 2NN bonds can be divided into two classes if we consider the Ir^{4+} network: (1) the 2NN sites which can be connected through *only one* common intermediate Ir^{4+} site, and (2) the 2NN sites that require traversing through *more than one* intermediate Ir^{4+}

[1] The relative sign between t_{xy} and t_z can be eliminated by transforming $c_i^\dagger \to -c_i^\dagger$ for $i \in (2,3)$ while the overall sign is inconsequential since the Hamiltonian is particle-hole symmetric.

site. In Sec. V, our microscopic derivation shows that, starting from a t_{2g} hopping model with 1NN hopping terms and taking the strong SOC limit, only the 12 2NN bonds belonging to the first class are nonzero in the effective $j_{\text{eff}} = \frac{1}{2}$ tight-binding model to lowest order. Hence, we shall only consider nonzero 2NN hopping for these 12 2NN bonds and neglect the rest in our tight-binding model. Generally, we can write

$$h_{ij}^{\text{2NN}} = t_{\text{2NN}}\mathbb{I} + i\left(\mathbf{v}_{ij}^{(1)} + \mathbf{v}_{ij}^{(2)}\right)\cdot\sigma, \tag{6}$$

where t_{2NN} is the scalar hopping and to bring out the analogy with the Kane-Mele model [27] on the two-dimensional honeycomb lattice, we have split the spin-dependent hopping into two parts. The first part is the three-dimensional version of the Kane-Mele term

$$\mathbf{v}_{ij}^{(1)} = v_{\text{KM}}\frac{\hat{r}_{ik}\times\hat{r}_{kj}}{|\hat{r}_{ik}\times\hat{r}_{kj}|}, \tag{7}$$

where v_{KM} is the strength of the coupling and $\mathbf{r}_{ik}$ and $\mathbf{r_{jk}} = (-\mathbf{r_{kj}})$ denote the vectors from the sites i and j, respectively, to their common nearest-neighbor site k. The second part of the vector hopping, not present on the 2D honeycomb lattice (due to the presence of a mirror symmetry), is normal to the first and is given by

$$\mathbf{v}_{ij}^{(2)} = v_{\parallel}\epsilon_{ij}\hat{\mathbf{r}}_{ij}, \tag{8}$$

where $v_{\parallel}$ is the strength of this coupling and $\epsilon_{ij} = \pm 1$ is appropriately chosen such that $\mathbf{v}_{ij}^{(2)}$ transforms as a pseudovector under lattice transformations as required by symmetry.

To conclude this section, we make a brief note on particle-hole symmetry of various limits. While the 1NN-only model is particle-hole symmetric as mentioned in Sec. III A, finite t_{2NN} and/or $v_{\parallel}$ hopping amplitudes will break such symmetry. On the other hand, the v_{KM} hopping amplitude preserves this symmetry, as we show explicitly in Appendix C. In other words, the 1NN plus finite v_{KM} model is particle-hole symmetric.

IV. PHASE DIAGRAM OF THE 2NN TIGHT-BINDING MODEL

In this section, we outline the generic phase diagram for the single-particle hopping Hamiltonian given by Eq. (1), where the different parameters are defined by Eqs. (3), (4), and (6). In Fig. 3, we present 2NN phase diagram with t_{2NN}, $v_{\parallel}$, and v_{KM} as the axes. We have set the 1NN hopping integrals to $t_{xy} = t_z = 1$ and $\theta = 0$. We note that the phase diagram is symmetric under $(t_{\text{2NN}}, v_{\text{KM}}, v_{\parallel}) \to -(t_{\text{2NN}}, v_{\text{KM}}, v_{\parallel})$ since this transformation merely inverts the electronic band structure (not shown). Hence, only $v_{\parallel} > 0$ is presented.

The orange regions indicate a strong topological insulator (STI) with Z_2 indices (1; 000), the blue regions indicate a metallic state, and the pink regions indicate a trivial band insulator (BI). The borders between STIs and BIs are semimetals. This is because time-reversal symmetry remains intact in both the phases therefore the electronic band gap in the bulk must close when the topology of the bands, as encapsulated by the Z_2 indices, changes. We note that finite t_{2NN} and/or $v_{\parallel}$ breaks the particle-hole symmetry of the band structure and hence the metallic states are generically present as opposed to the 1NN case. In the special case where $|t_{\text{2NN}}|$ is small and $v_{\text{KM}} = v_{\parallel} = 0$, the ground state is a metallic phase with a line-node Fermi surface akin to the metallic phase found in the 1NN-only model. As $|t_{\text{2NN}}|$ increases while $v_{\text{KM}} = v_{\parallel} = 0$, bands approach and cross the Fermi level, thus generating particle and hole pockets. This displaces the line node away from the Fermi level and yields a metallic state with particle pockets.

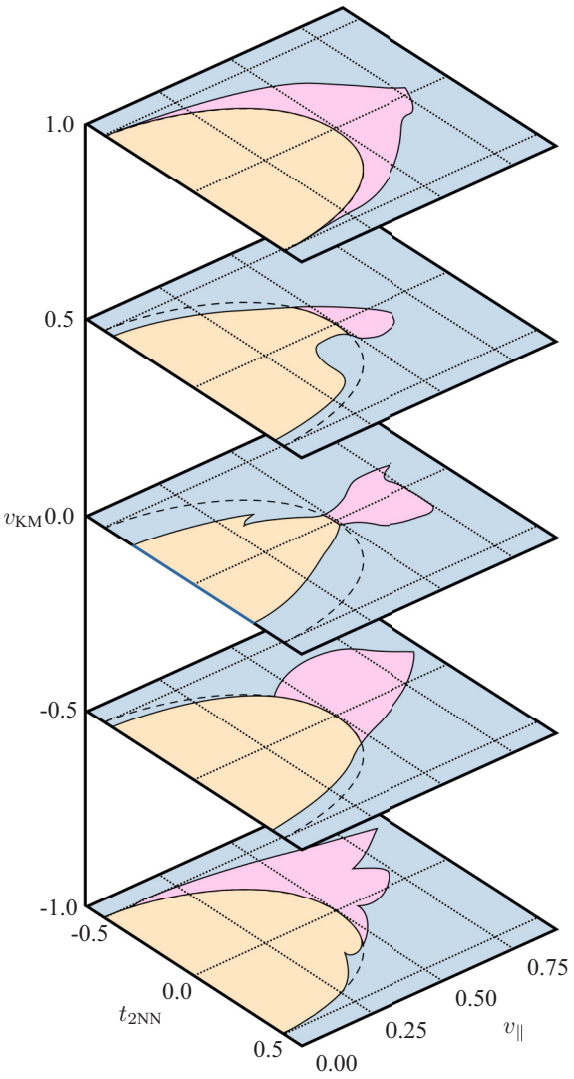

FIG. 3. (Color online) Phase diagram in the noninteracting limit with 2NN hopping amplitudes with slices in the v_{KM} direction. Nearest-neighbor hopping amplitudes have been set to $t_{xy} = t_z = 1$, $v_z = 0$. Orange is a strong topological insulator, blue is a metal, and pink is a trivial band insulator. The dotted semicircle indicates the region in which any insulating state must be a STI, and outside of which any insulating state must be trivial (see main text for explanation). The blue line along $v_{\text{KM}} = v_{\parallel} = 0$ is a metallic state with a line-node Fermi surface akin to the metallic state in the 1NN-only model.

We draw attention to the region within $t_{\text{2NN}}^2 + v_{\parallel}^2 \leqslant 0.5^2$ (in units of t_{xy}, indicated by dashed lines in Fig. 3), where the STI and metallic phases exist but not the BI phase. On the other hand, the BI and metallic phases can be found outside this region but not the STI phase. To understand this, we note that the strong Z_2 index is calculated from the product

of the parity eigenvalues [25] at the time-reversal-invariant momentum (TRIM) points of the Brillouin zone (BZ) since inversion symmetry is present. Out of the eight TRIM points in the three-dimensional BZ, we find that the product of the parity eigenvalues changes only at the Γ point as we move from a STI to a trivial band insulator. Thus, we expect that the mass inversion affects only the product of the parity eigenvalues at the Γ point. We find that the parameter controlling this band inversion, and hence the parity eigenvalues, depends only on $t_{2\mathrm{NN}}$ and $v_{\parallel}$ but not on v_{KM}. In fact, when $t_{2\mathrm{NN}} = v_{\parallel} = 0$ and $v_{\mathrm{KM}} \neq 0$, the insulating phase is always a STI. The accidental degeneracy that closes the band gap at the Γ point occurs precisely when $t_{2\mathrm{NN}}^2 + v_{\parallel}^2 = 0.5^2$; a gap opens if we deviate from this curve. Therefore, any insulating phase within $t_{2\mathrm{NN}}^2 + v_{\parallel}^2 \leqslant 0.5^2$ must have the same strong Z_2 topological index as the case of $t_{2\mathrm{NN}} = v_{\parallel} = 0$ and $v_{\mathrm{KM}} \neq 0$, i.e., a STI, whereas any insulating phase outside of this region *can* be topologically distinct, as in this case a BI. The nature of the metallic states depends on the local features of the band structure like the presence of particle or hole pockets where the chemical potential crosses the Fermi level.

V. MICROSCOPIC CONSIDERATIONS: DERIVATION OF A $j_{\mathrm{eff}} = \frac{1}{2}$ MODEL FROM A MULTIORBITAL t_{2g} MODEL IN THE STRONG SPIN-ORBIT COUPLING LIMIT

Having derived the general symmetry-allowed tight-binding model in Sec. III, here we explore a microscopic multiorbital t_{2g} tight-binding model with SOC on the ideal hyperhoneycomb lattice within the Slater-Koster approximation [28]. As noted earlier, unlike the generic tight-binding model considered in the previous sections where oxygen and iridium distortions are encapsulated in quantitative changes in the $j_{\mathrm{eff}} = \frac{1}{2}$ hopping amplitudes, here we specialize in the case where both the iridium and oxygen ions are in their ideal positions. This implies that each iridium ion is surrounded by a perfect oxygen octahedron, all 1NN bonds are of equal length, and the Ir-Ir-Ir and Ir-O-Ir bond angles are 120° and 90°, respectively. With these assumptions and in the limit of large SOC, we will show the connection between the microscopic tight-binding model and the generic symmetry-allowed tight-binding model presented in Sec. III, particularly the relations between the microscopic Slater-Koster parameters and the hopping parameters introduced earlier. The results of this section will provide us with valuable insights in the understanding of the DFT results in the next section.

In the ideal hyperhoneycomb lattice, each Ir ion resides in a perfect octahedral cage of oxygen ions. The resulting crystal field causes the Ir d orbitals to split into the lower-energy t_{2g} orbitals and the higher-energy e_g orbitals with energy difference on the order of a few electron volts. When SOC and hopping amplitudes are much smaller than the crystal-field energy splitting, the e_g orbitals can be projected since the five electrons at each Ir^{4+} site will mostly contain t_{2g} character. The atomic SOC, when projected on the t_{2g} orbitals, has the following form:

$$H_{\mathrm{SOC}} = -\sum_i \lambda \vec{L}_i \cdot \vec{S}_i, \tag{9}$$

where $\vec{L}_i$ transforms as an angular momentum one operator (with the three L_z components being linear combinations of the three t_{2g} orbitals [29]), $\vec{S}_i$ is the spin of a single electron occupying the t_{2g} orbitals, and $\lambda(\sim 500$ meV) is the strength of the atomic SOC. Due to the negative sign [29], the $j_{\mathrm{eff}} = \frac{1}{2}$ orbitals are higher in energy than the $j_{\mathrm{eff}} = \frac{3}{2}$ orbitals.

We consider two types of hopping amplitudes between 1NN iridium ions within the Slater-Koster approximation: the direct overlap between adjacent Ir t_{2g} orbitals and the indirect hopping mediated by the two shared oxygen ions in the edge-shared oxygen octahedra configuration. The resulting tight-binding model in the t_{2g} basis can be written as

$$H_{t_{2g}} = \sum_{\langle ij \rangle} d_i^{\dagger} \left[h_{ij}^{\mathrm{direct}}(t_\sigma, t_\pi, t_\delta) + h_{ij}^{\mathrm{indirect}}(t_{\mathrm{oxy}}) \right] d_j, \tag{10}$$

where $d^{\dagger} = (d_{yz}^{\dagger}, d_{xz}^{\dagger}, d_{xy}^{\dagger})$ are the creation operators in the t_{2g} basis. The direct hopping matrix h_{ij}^{direct} is parametrized by Slater-Koster parameters t_σ, t_π, and t_δ representing σ, π, and δ hopping amplitudes between adjacent t_{2g} orbitals, respectively. The indirect hopping matrix $h_{ij}^{\mathrm{indirect}}$ is parametrized by $t_{\mathrm{oxy}} = |t_{pd\pi}|^2/\Delta$, where $t_{pd\pi}$ is the π hopping between iridium d orbitals and oxygen p orbitals and Δ is the energy difference between those two sets of orbitals. The detailed form of the hopping matrices is outlined in Appendix D.

In the large SOC limit, the bands arising from the $j_{\mathrm{eff}} = \frac{1}{2}$ and the $j_{\mathrm{eff}} = \frac{3}{2}$ orbitals are expected to separate. In the $\lambda \to \infty$ limit, an effective tight-binding model involving only the $j_{\mathrm{eff}} = \frac{1}{2}$ degrees of freedom can be obtained by lowest-order perturbation theory: projection of the t_{2g} bands into the $j_{\mathrm{eff}} = \frac{1}{2}$ manifold

$$H_{\mathrm{eff}}^{(1)} = \mathcal{P} H_{t_{2g}} \mathcal{P}, \tag{11}$$

where $\mathcal{P}$ is the projector for the $j_{\mathrm{eff}} = \frac{1}{2}$ manifold. This projection yields a 1NN $j_{\mathrm{eff}} = \frac{1}{2}$ model with

$$t_{xy}^{1\mathrm{NN}} = t_z^{1\mathrm{NN}} = (3t_\sigma + 4t_\pi + 5t_\delta)/6; \quad \left| v_z^{1\mathrm{NN}} \right| = 0. \tag{12}$$

As discussed in Sec. III A, this effective Hamiltonian is particle-hole symmetric and can only host a metallic phase with a line-node Fermi surface. In addition, the model is manifestly SU(2) invariant despite the presence of SOC. Lastly, oxygen-mediated hopping does not contribute at this order. This is because the amplitudes from the two oxygen-mediated hopping paths cancel exactly under projection into the $j_{\mathrm{eff}} = \frac{1}{2}$ manifold when Ir-O-Ir bond angles are 90°. Clearly, the above model does not represent the general structure and the next order correction arising from finite values of λ must be considered to better describe the band structure obtained in the original t_{2g} model.

Including the second-order term in perturbation theory, the effective Hamiltonian can be written as

$$H_{\mathrm{eff}} = H_{\mathrm{eff}}^{(1)} + H_{\mathrm{eff}}^{(2)} + \mathcal{O}\left(\frac{H_{t_{2g}}^3}{(3\lambda/2)^2} \right), \tag{13}$$

with

$$H_{\mathrm{eff}}^{(2)} = (3\lambda/2)^{-1} \mathcal{P} H_{t_{2g}} \mathcal{Q} H_{t_{2g}} \mathcal{P}, \tag{14}$$

where $\mathcal{Q}$ is the projector for the $j_{\rm eff} = \frac{3}{2}$ manifold. In addition to 1NN hopping generated from $H^{(1)}_{\rm eff}$, the second-order term $H^{(2)}_{\rm eff}$ now generates 2NN hopping amplitudes via virtual hopping to $j_{\rm eff} = \frac{3}{2}$ orbitals at intermediate Ir sites. The generated 2NN hopping amplitudes take the form of those considered in Sec. III B, hence, we can relate the Slater-Koster parameters used in this section with those used in the generic symmetry-allowed tight-binding model. The relations, including the contribution from $H^{(1)}_{\rm eff}$, are given by

$$\begin{aligned} |v_z| &= 0, \\ t_{xy} &= t_z = (3t_\sigma + 4t_\pi + 5t_\delta)/6, \\ t_{\rm 2NN} &= -(3t_\sigma - 2t_\pi - t_\delta)^2/(108\lambda), \\ v_{\rm KM} &= (t_\pi - t_\delta - 2t_{\rm oxy})(3t_\sigma - 3t_\pi + 2t_{\rm oxy})/(9\sqrt{3}\lambda), \\ v_\parallel &= (t_\pi - t_\delta - 2t_{\rm oxy})(3t_\sigma - 3t_\delta - 4t_{\rm oxy})/(9\sqrt{6}\lambda). \end{aligned} \tag{15}$$

We note that by assuming an ideal hyperhoneycomb lattice structure together with truncating the perturbation series at second order, the 1NN xy and z bonds have the same scalar-only hopping amplitude. Furthermore, truncating the perturbation series at second order implies that 2NN hopping amplitudes are only generated on 2NN bonds with shared Ir sites. These 2NN bonds, although not related by symmetry, have related hopping amplitudes because of the assumed ideal structure and the truncated perturbative series (see Appendix B for details). Since the higher-order terms in the series fall off as an inverse power of the SOC coupling, we expect that these higher-order terms are small in magnitude and hence may be negligible to the leading order.

By establishing the t_{2g} tight-binding model in the Slater-Koster approximation, we can perform a loose fit against *ab initio* calculations to obtain an estimate of these hopping amplitudes as we show in the next section. Furthermore, by relating the Slater-Koster parameters with hopping amplitudes used in the generic tight-binding model, short-ranged electronic correlation can be included straightforwardly in the effective $j_{\rm eff} = \frac{1}{2}$ model as we exemplify in Sec. VII.

VI. *AB INITIO* CALCULATIONS ON β-Li_2IrO_3 IN THE IDEAL STRUCTURE AND CONNECTION TO THE TIGHT-BINDING MODEL

Having discussed the details of the tight-binding models, we now employ approaches for the ideal β-Li_2IrO_3 structure and try to capture its characteristic features via the tight-binding model introduced in the previous section. At the outset, we note that in the absence of data determining the accurate lattice structure of β-Li_2IrO_3, we have assumed that it has ideal structure and the oxygen octahedra are not distorted. While this structure may not be an accurate description of the material, it gives us an idea of the general validity of the approximations made in the two earlier sections about the $j_{\rm eff} = \frac{1}{2}$ nature of the bands near the Fermi level. Also, we can obtain a qualitative estimate of the various parameters used in the previous two tight-binding models. We look for general features that may aid the determination of the parameter regime of the tight-binding Hamiltonian which is of interest in the context of materials.

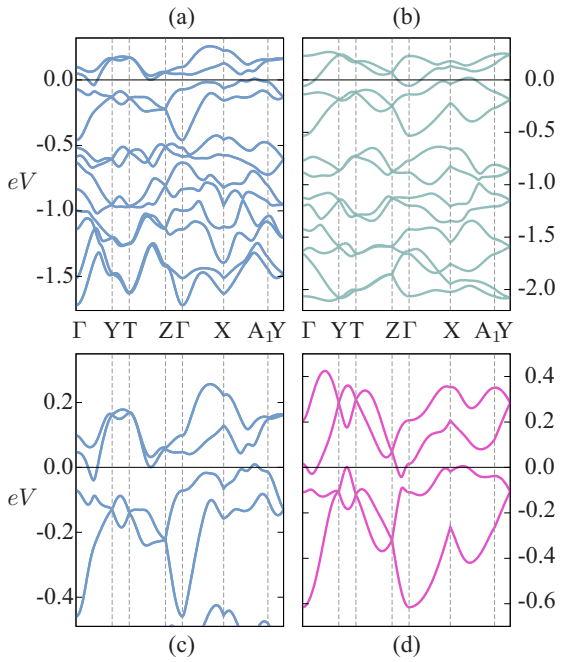

FIG. 4. (Color online) Electron band structures of ideal β-Li_2IrO_3 and tight-binding fit. (a) t_{2g} bands from the DFT calculation. (b) t_{2g} tight-binding model with the parameter in Eq. (16). (c) Top eight t_{2g} ($j_{\rm eff} = \frac{1}{2}$) bands in (a). (d) $j_{\rm eff} = \frac{1}{2}$ tight-binding model with the parameter in Eq. (17). In the above plots, the Fermi level is at 0 eV, the DFT bands are plotted in blue, the tight-binding t_{2g} bands in green, and the tight-binding $j_{\rm eff} = \frac{1}{2}$ bands in red. Each band is doubly degenerate due to time-reversal and inversion symmetry.

Figure 4(a) shows 12 t_{2g} bands from the DFT calculation for the ideal β-Li_2IrO_3 using OPENMX [30] in which the linear-combination-of-pseudo-atomic-orbital formalism and a fully relativistic j-dependent pseudopotential in a noncollinear methodology are adopted. The Perdew-Burke-Ernzerhof generalized gradient approximation (GGA) functional was used for the exchange-correlation energy [31], and 300 Ry of energy cutoff and the $12 \times 12 \times 12$ Monkhorst-Pack grid are used for the real- and the momentum-space integrations, respectively. Each of the 12 bands is doubly degenerate due to time-reversal and inversion symmetries. A remarkable feature of the bands near the Fermi level is their pronounced $j_{\rm eff} = \frac{1}{2}$ character. As the density of states (DOS) of the band structure shows (Fig. 5), the upper four bands ($\gtrsim -0.5$ eV) have strong $j_{\rm eff} = \frac{1}{2}$ orbital character, while the bottom eight bands ($\lesssim -0.5$ eV) have

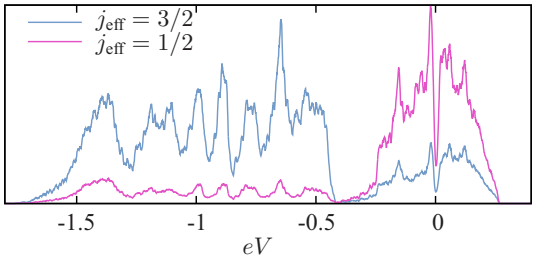

FIG. 5. (Color online) Density of states for the DFT band structure in Fig. 4(a). The density of states is projected into the $j_{\rm eff} = \frac{1}{2}$ (red) and $j_{\rm eff} = \frac{3}{2}$ (blue) orbital sectors.

main contributions coming from $j_{\rm eff}=\frac{3}{2}$ orbitals. Hereafter, we call the former $j_{\rm eff}=\frac{1}{2}$ bands and the latter $j_{\rm eff}=\frac{3}{2}$ bands. Another notable result is that the ideal β-Li_2IrO_3 structure is in a metallic phase in the noninteracting limit. The Fermi level crosses the $j_{\rm eff}=\frac{1}{2}$ bands generating several Fermi pockets along the lines Γ-Y, T-Z, X-A_1, etc. [see Fig. 4(c)].

The predominant $j_{\rm eff}=\frac{1}{2}$ character of the bands near the Fermi level strongly supports our assumption that the low-energy electronic degrees of freedom can be adequately described by $j_{\rm eff}=\frac{1}{2}$ orbitals. In turn, this lends credence to our use of the $j_{\rm eff}=\frac{1}{2}$ tight-binding model in the previous sections when modeling Ir-based hyperhoneycomb compounds.

Next, we fit the t_{2g} model in Eq. (10) to the DFT results by adjusting the Slater-Koster parameters. Figure 4(b) shows the resulting electronic bands of the t_{2g} model, which has the following hopping parameters:

$$\begin{aligned} t_\sigma &= -0.4574\ \text{eV}, \quad t_\pi = 0.6098\ \text{eV},\\ t_\delta &= -0.0041\ \text{eV}, \quad t_{\rm oxy} = 0.1155\ \text{eV}. \end{aligned} \tag{16}$$

In our fitting process, we adopted $\lambda = 0.5797$ eV from Ref. [32] and adjusted the other parameters t_σ,t_π,t_δ, and $t_{\rm oxy}$. The tight-binding model reproduces two overall features found in the DFT computation: (1) well separated $j_{\rm eff}=\frac{1}{2}$ (top four) and $j_{\rm eff}=\frac{3}{2}$ (bottom eight) bands and (2) a semimetallic phase, albeit with pockets at different positions from those found in the DFT. However, quantitative details like correct band curvatures and energy values are not recovered within our model, indicating that further neighbor hopping amplitudes are required for a quantitatively better fit. According to our Wannier function analysis within DFT [33], it is necessary to include up to fourth-nearest-neighbor hopping amplitudes in the tight-binding model to recover the quantitative features of the DFT band structure, thus we should take our tight-binding fit as a "loose" fit that aims not to replicate exact details, but to reproduce qualitative features of the DFT results. Among the hopping amplitudes up to the fourth-nearest neighbors, the 1NN hopping amplitudes have the largest magnitudes and determine the overall behavior of the band structure while further neighbor hopping amplitudes, which have relatively small magnitudes, are responsible for detailed structures. This justifies the calculations in the previous section where we have only taken the 1NN hopping amplitude in the t_{2g} Hamiltonian to be nonzero.

By mapping the t_{2g} model obtained from the fitting procedure to the effective $j_{\rm eff}=\frac{1}{2}$ model in Eq. (13), we arrive at the following values for the hopping amplitudes via the relations given in Eq. (15):

$$\begin{aligned} t_{xy,z} &= 0.1744\ \text{eV},\\ t_{\rm 2NN} &= -0.1150\ \text{eV},\\ v_{\rm KM} &= -0.1331\ \text{eV},\\ v_\parallel &= -0.0222\ \text{eV}, \end{aligned} \tag{17}$$

which corresponds to a point in the metallic region of Fig. 3, with $t_{\rm 2NN}^2+v_\parallel^2 > 0.5^2$. The band structure of the resulting $j_{\rm eff}=\frac{1}{2}$ model is plotted in Fig. 4(d) for comparison with the band structures of the t_{2g} model and DFT results.

This concludes our discussions on the electronic structure. Following, we shall investigate the effect of correlations in stabilizing magnetic ordering in the intermediate correlation regime.

VII. MAGNETIC ORDER AT INTERMEDIATE COUPLING

In several iridate compounds where the $5d^5$ iridium ions are octahedrally coordinated with oxygen ions, magnetic ordering often occurs at the iridium sites due to short-ranged electronic correlations [6]. As correlations are increased, the system changes from a paramagnetic metal to a magnetically ordered metal which at higher correlations becomes an insulator. In certain instances, the magnetic ordering and the metal-insulator transitions have been observed to occur simultaneously.

Here, we explore this scenario in the intermediate-coupling regime on the hyperhoneycomb lattice via self-consistent mean-field theory of the $j_{\rm eff}=\frac{1}{2}$ model. Starting with the 2NN tight-binding model outlined in Eq. (13), we include correlation effects via onsite Hubbard repulsion

$$U\sum_i n_{i\uparrow}n_{i\downarrow} = -\frac{2U}{3}\sum_i \mathbf{J}_i\cdot\mathbf{J}_i + \frac{U}{2}\sum_i n_i, \tag{18}$$

where $U>0$ is the Hubbard repulsion strength, $n_{i\sigma}$ is the number operator at site i with pseudospin σ, $n_i=\sum_\sigma n_{i\sigma}$, and $\mathbf{J}_i$ is the $j_{\rm eff}=\frac{1}{2}$ pseudospin operator. The local magnetic moment, when projected into the $j_{\rm eff}=\frac{1}{2}$ manifold, is proportional to the local $j_{\rm eff}=\frac{1}{2}$ moment, i.e., $\mathbf{M}_i=-2\mathbf{J}_i$. Hence, a Hartree-Fock decoupling of the $\mathbf{J}_i\cdot\mathbf{J}_i$ term will yield a mean-field Hamiltonian that can be self-consistently solved for the magnetic ordering of the $j_{\rm eff}=\frac{1}{2}$ moments. In the absence of compelling experimental motivation to choose particular hopping amplitudes, we choose a cut which interpolates between the purely isotropic 1NN model and the tight-bonding model whose parameters are given by our DFT calculations in Eq. (17). This is done in the following way: we choose

$$\begin{aligned} t_{xy,z} &= 0.1744\ \text{eV},\\ t_{\rm 2NN} &= (-0.1150\ \text{eV})x,\\ v_{\rm KM} &= (-0.1331\ \text{eV})x,\\ v_\parallel &= (-0.0222\ \text{eV})x \end{aligned} \tag{19}$$

and then vary x between 0 and 1 to interpolate between the two above limits. With this particular choice of hopping amplitudes, we are able to explore the effects of correlation on both the STI phase ($x \lesssim 0.74$) and the metallic phase ($x \gtrsim 0.74$).

To perform the self-consistent mean-field calculations, we consider four 3-component order parameters, $\langle\mathbf{J}_i\rangle$ with $i=1\ldots4$, and assume $\mathbf{q}=\mathbf{0}$ order.[2] The self-consistent solution

[2]We have explicitly checked that the spin model obtained in the strong-coupling expansion of our Hubbard model always yielded the same $\mathbf{q}=\mathbf{0}$ magnetic order as our mean-field results within the parameter regime we considered. Moreover, this magnetic order remains the ground state for a broad range of parameters in the spin model as long as the 2NN spin-spin interactions remain moderately small. This fact gives us reason to believe that $\mathbf{q}=\mathbf{0}$ ansatz in our mean-field calculation may be a reasonable simplification.

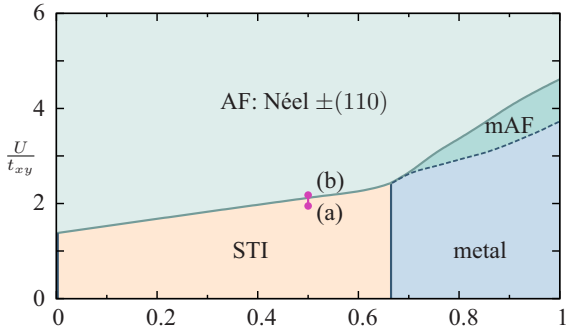

FIG. 6. (Color online) Phase diagram at finite Hubbard repulsion U as a function of 2NN hopping strength x (see text for description of 2NN hopping used). The local magnetic moments of the Néel state (AF) and the metallic magnetically ordered phase (mAF) point in the ±(110) direction. The solid line between the strong topological insulator (STI) and the AF state indicates a second-order transition, while the dashed line between the metal and the mAF phases indicates a first-order transition. The transition from the mAF phase to the AF state is continuous. The $x = 0$ line describes a purely 1NN model where the paramagnetic ground state has a line-node Fermi surface, as indicated by the blue line. The two points (a) and (b) indicate where the slab configurations were computed in Fig. 7.

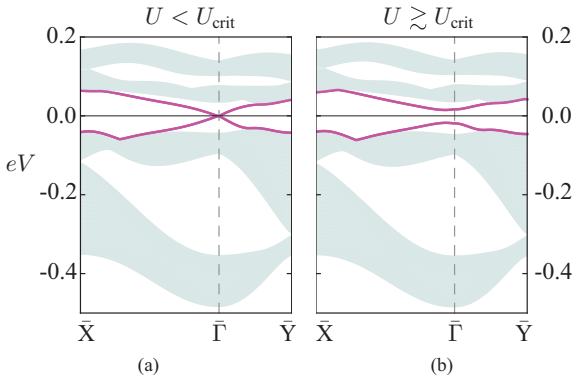

FIG. 7. (Color online) Gapping out the gapless surface states. For illustration, we present surface states from a slab configuration. Purple bands are surface states while the shaded regions are the projected bulk bands. We have set 2NN hopping amplitudes to be $x = 0.5$ (see main text for definition and Fig. 6 for reference). The system undergoes a second-order transition from a strong topological insulator (STI) to a magnetically ordered phase (AF) at $U_{\text{crit}} \simeq 2.12 t_{xy}$. In (a), $U < U_{\text{crit}}$, the ground state is a STI and a surface Dirac cone is seen at $\bar{\Gamma}$. In (b), U is slightly above U_{crit}, the ground state is the AF phase, and the surface Dirac cone develops a finite gap.

is achieved with no constraints on the magnetic configuration such that all $\mathbf{q} = \mathbf{0}$ ordering can be sampled in principle.

In Fig. 6, we present the finite-U phase diagram as a function of 2NN hopping amplitudes. Upon increasing $U/t_{xy} \gtrsim 1.4$–3.4, the time-reversal-symmetric phases undergo phase transitions to an antiferromagnetic, Néel ordered phase with magnetic moments pinned along the $+\hat{x} + \hat{y}$ direction (light green). From the STI (orange), the phase transition is of second order. On the other hand, starting with the metallic phase (blue), a first-order transition is observed. This first-order transition initially brings the system into a magnetically ordered metallic phase (mAF, dark green), then upon further increase in U, the system acquires a finite excitation gap and becomes insulating. This metal-insulator transition is continuous in the magnetic order parameters. We also note that at $x = 0$, the model reduces to a purely 1NN model and the paramagnetic phase is metallic with a line-node Fermi surface as outlined in Sec. III A. This phase is indicated as the vertical blue line at $x = 0$ running along the U/t_{xy} axis.

Although this magnetic order breaks inversion symmetry ($\mathcal{P}$) of the lattice, it preserves inversion followed by time-reversal symmetry ($\mathcal{P}\Theta$). Since $\mathcal{P}(\mathbf{k})$ commutes with $\Theta(\mathbf{k})$ for all $\mathbf{k}$ in the Brillouin zone of the hyperhoneycomb lattice, a pseudo-Kramers degeneracy is present at all momenta. Instead of the usual Kramers degeneracy where Θ protects the degeneracy and together with $\mathcal{P}$ ensure at least doubly degenerate bands, these pseudo-Kramers bands are protected by the combined operation $\mathcal{P}\Theta$.

With $\mathcal{P}\Theta$ playing the role of a preserved antiunitary symmetry, the magnetically ordered state may harbor nontrivial topology in the spirit of Refs. [34–37]. However, in the present case, we find that the magnetic phase has a trivial band structure and there are no gapless surface states arising from nontrivial band topology. We show this in Fig. 7, where band-structure calculations in a slab configuration are presented with 2NN hopping amplitudes set to $x = 0.5$. Here, the $\mathbf{a}_1$ direction (see Fig. 1) has finite spatial extent.[3] While in the STI phase, the surface Dirac cone at the $\bar{\Gamma}$ point can be seen. However, upon increasing U through the second-order transition, the surface Dirac cone becomes fully gapped (nearby momentum points were also checked to assure that the gap was fully developed).

VIII. DISCUSSION AND OUTLOOK

In this work, we have investigated the weak- and intermediate-coupling regimes of iridium-based compounds on the hyperhoneycomb lattice. Using a combination of symmetry arguments and a more microscopic calculation based on the Slater-Koster approximation, we have determined the low-energy electronic structure for the $j_{\text{eff}} = \frac{1}{2}$ orbitals by explicitly constructing a tight-binding model. Such orbitals are expected to dominate the low-energy physics of Ir due to strong SOC. Our DFT calculations for β-Li_2IrO_3 support this expectation by showing that the bands near the Fermi level indeed have a $j_{\text{eff}} = \frac{1}{2}$ character.

It was shown that the 1NN-only tight-binding model admits a trivial insulating phase as well as a semimetallic phase with a line-node Fermi surface. This semimetallic phase becomes a STI upon gapping out the line node when 2NN hopping amplitudes are introduced. Ultimately, the tight-binding model up to 2NN contains both trivial as well as topological band insulators in addition to a metallic phase.

We study the effects of Hubbard-type electronic correlations on the above band structure, particularly in the stabilization of magnetic order. Restricting ourselves to $\mathbf{q} = \mathbf{0}$ magnetic orders, we perform Hartree-Fock calculations and

[3]Similar results from slab calculations with finite spatial extent in the $\mathbf{a}_2$ and $\mathbf{a}_3$ have also been obtained, but not shown.

determine the mean-field phase diagram. Our calculations admit a direct continuous phase transition between the STI and the Néel ordered magnetic insulator as we turn on correlations. The magnetic insulator breaks both time-reversal symmetry and inversion symmetry independently, but it preserves the product of the two. Although not realized within the current parameter regime, this raises a possibility of a concrete microscopic model on the hyperhoneycomb lattice where such an antiunitary symmetry (product of time reversal and inversion) may stabilize a nontrivial topological band structure for the electrons in the presence of interactions. We also note that while our calculations have been directly motivated by the recent discovery of β-Li_2IrO_3, the results presented here are not necessarily restricted to this particular material.

It is instructive to consider the range of applicability of our current work and contrast it with previous approaches. Previous works on Ir-based compounds on the hyperhoneycomb lattice studied the Heisenberg-Kitaev spin Hamiltonian, which may be applicable in the strong-coupling regime [19–21,38]. In these works, the correlation effects of Hund's coupling is paramount to the presence of the Kitaev interaction from a microscopic perspective [1,4,7]. Implicit in the derivation is the assumption of $U > (J_H, \lambda) \gg t$ where J_H is Hund's coupling and t is the typical hopping amplitude. In contrast, in Sec. VII of this work, we considered the intermediate-coupling limit where $\lambda \approx U \approx t \gg J_H$ such that the effects of $j_{\text{eff}} = \frac{3}{2}$ states can be treated perturbatively and that Hund's coupling can be ignored. In addition, other theoretical approaches have been explored in other iridate compounds [39–41]. Indeed, these ideas could stimulate interesting future research directions in the theoretical study of β-Li_2IrO_3.

Although the definitive structure of β-Li_2IrO_3 is presently not known, the $j_{\text{eff}} = \frac{1}{2}$ orbitals may still be the lowest-energy degree of freedom under sufficiently small distortions and nonoctahedral crystal-field effects [42,43]. If further-neighbor hopping amplitudes are negligible, the tight-binding calculations presented in Sec. III will be applicable, although the parameters in the more microscopic calculations may be affected. If distortions are small, however, the results of our microscopic calculations may have captured the essential qualitative features present in the electronic structure β-Li_2IrO_3 and other, yet-to-be-discovered, isostructural iridate compounds. Furthermore, the magnetic order that may be present in these compounds may be well described by our mean-field calculations if the material lies within the intermediate-coupling regime. In this regard, we believe that our results serve as a valuable starting point in the description of these fascinating compounds.

ACKNOWLEDGMENTS

We thank S.-B. Lee and V. Vijay Shankar for discussions. This research was supported by the NSERC, CIFAR, and Centre for Quantum Materials at the University of Toronto. H.-S. Kim was supported by Basic Science Research Program through the National Research Foundation of Korea (NRF) funded by the Ministry of Education (Grant No. 2013R1A6A3A01064947). H. Jin is supported by the Research Center Program of the Institute for Basic Science in Korea.

APPENDIX A: HYPERHONEYCOMB LATTICE

The space group of the hyperhoneycomb lattice is $Fddd$. The Ir ions occupy the Wyckoff position 16e, which possesses a site symmetry of C_2. These C_2 axes coincide with the z bonds and can be used to relate x and y bonds. In addition, the positions of the Ir ions imply that the bond center of the z bonds is located at the Wyckoff position 8a, which possesses the site symmetry group D_2 with three C_2 axes, while the bond center of the x and y bonds are located at the Wyckoff position 16c, which are inversion centers of the lattice. By assigning each Ir site with orbitals that transform like a spinor (e.g., $j_{\text{eff}} = \frac{1}{2}$ orbitals), the bond-center symmetry operations outlined above constrains the 1NN tight-binding model to take the form outlined in Sec. III A. The 2NN bonds, on the other hand, are less constrained by symmetry and will be discussed separately in Appendix B.

APPENDIX B: SECOND-NEAREST NEIGHBORS

In the ideal hyperhoneycomb, there are four symmetry-inequivalent sets of 2NN bonds of equal bond length. As mentioned in Sec. III B, these bonds can first be classified as those that can be connected by traversing through only one intermediate Ir site (type 1; there are 12 such bonds), and those that can not (type 2; there are 8 such bonds). Furthermore, type 1 can be split into two sets: bonds of type 1a connect different sublattices of the same parity (i.e., 1 with 3, 2 with 4; there are eight of these) while bonds of type 1b connect same sublattices (i.e., 1 with 1, etc.; there are four of these). Type-2 bonds are also split into two additional subclasses: bonds of type 2a connect sublattices of different parity (i.e., 1 with 4, 2 with 3; there are four of these) while bonds of type 2b connect same sublattices (i.e., 1 with 1, etc.; there are four of these). These four types of 2NN bonds are inequivalent in that no symmetry operation can relate bonds of different types.

The symmetry operations at the bond centers constrain the terms that can appear in the $j_{\text{eff}} = \frac{1}{2}$ tight-binding model. For type 1a, the bond center does not possess any site symmetries, hence the vector hopping along this bond can have three independent components. For type 1b, the bond center has a C_2 symmetry, hence we can choose to parametrize the two independent components of the vector hopping with v_{KM} and $v_{\parallel}$ as outlined in Sec. III B. From symmetry analysis, type-1a and type-1b bonds are unrelated. However, in the ideal hyperhoneycomb, the *local* oxygen and lithium environments of these two types of bonds are identical (local as defined by nearest neighbors to the Ir sites of the bond). Treating nonlocal ions as negligible symmetry-breaking terms, we can use the mirror operation that relates these two bond environments to relate the vector hopping of type 1a to that of type 1b. This simplification was used in parametrizing the 2NN bonds in Sec. III B and is manifest in Sec. V.

For bonds of type 2a, there exists a C_2 symmetry operation which reduces the vector hopping amplitude to two components. For bonds of type 2b, the bond center is an inversion center and hence only scalar hopping is allowed. Bonds of type 2 were not included in our model: this is motivated by our microscopic derivation in Sec. V.

APPENDIX C: PARTICLE-HOLE SYMMETRY

We consider particle-hole-symmetry transformations of the following form:

$$\begin{aligned} c_{i\sigma} &\to c_{i\sigma}^{\dagger} \quad \text{for} \quad i \in 1,3, \\ c_{i\sigma} &\to -c_{i\sigma}^{\dagger} \quad \text{for} \quad i \in 2,4. \end{aligned} \tag{C1}$$

We first consider scalar hopping terms. The 1NN scalar hopping terms in Eqs. (3) and (4) transform as

$$t_{\alpha}(c_{i\sigma}^{\dagger}c_{j\sigma} + \text{H.c.}) \to t_{\alpha}(c_{i\sigma}^{\dagger}c_{j\sigma} + \text{H.c.}), \tag{C2}$$

where α stands for the x, y, or z bonds. This shows that 1NN scalar hopping terms are invariant. The 2NN scalar hopping

$$t_{2\text{NN}}(c_{i\sigma}^{\dagger}c_{j\sigma} + \text{H.c.}) \to -t_{2\text{NN}}(c_{i\sigma}^{\dagger}c_{j\sigma} + \text{H.c.}) \tag{C3}$$

is not invariant. Hence, the $t_{2\text{NN}}$ term breaks particle-hole symmetry.

Vector hopping terms take the form

$$i(c_i^{\dagger}\mathbf{v}_{ij}\cdot\sigma c_j + c_j^{\dagger}\mathbf{v}_{ji}\cdot\sigma c_i) \tag{C4}$$

with $\mathbf{v}_{ji} = -\mathbf{v}_{ij}$ an $\mathbf{v}_{ij} \in \mathbb{R}$. For the above particle-hole transformation followed by a global U(1) spin rotation,

$$c_i \to e^{-i\frac{\pi}{4}\sigma^z}c_i, \tag{C5}$$

we find that the 1NN vector hopping amplitude as well as the Kane-Mele type of 2NN vector hopping amplitude in Eq. (7) are invariant under the combined transformation. However, the second contribution to the 2NN vector hopping given by Eq. (8) is not. Since the U(1) rotation is global, it does not affect the invariance of the scalar hopping amplitudes discussed above.

APPENDIX D: HOPPING AMPLITUDES IN THE t_{2g} MODEL

The hopping amplitudes between 1NN can be broken up into contributions from the direct overlap of adjacent Ir t_{2g} orbitals and oxygen-mediated hopping. On the z bond, the former, as parametrized by Slater-Koster parameters, is given by

$$h_z^{\text{direct}} = \begin{pmatrix} (t_\pi + t_\delta)/2 & (t_\pi - t_\delta)/2 & 0 \\ (t_\pi - t_\delta)/2 & (t_\pi + t_\delta)/2 & 0 \\ 0 & 0 & (3t_\sigma + t_\delta)/4 \end{pmatrix}, \tag{D1}$$

and the latter is given by

$$h_z^{\text{indirect}} = \begin{pmatrix} 0 & -t_{\text{oxy}} & 0 \\ -t_{\text{oxy}} & 0 & 0 \\ 0 & 0 & 0 \end{pmatrix}, \tag{D2}$$

where the basis used is given by $d^{\dagger} = (d_{yz}^{\dagger}, d_{xz}^{\dagger}, d_{xy}^{\dagger})$. The Slater-Koster parameters t_σ, t_π, and t_δ represent σ, π, and δ hopping amplitudes between adjacent t_{2g} orbitals, respectively. The oxygen-mediated hopping is given by $t_{\text{oxy}} = |t_{pd\pi}|^2/\Delta$, where $t_{pd\pi}$ is the π hopping between iridium d orbitals and oxygen p orbitals and Δ is the energy difference between those two sets of orbitals. In the ideal hyperhoneycomb lattice, the *local* environment surrounding the z and x/y bonds are related by C_3 rotations about the (111) direction, hence the hopping amplitudes on the x/y bonds can be obtained by rotating the above hopping matrices in the appropriate manner.

[1] G. Jackeli and G. Khaliullin, Phys. Rev. Lett. **102**, 017205 (2009).
[2] B.-J. Yang and Y. B. Kim, Phys. Rev. B **82**, 085111 (2010).
[3] D. Pesin and L. Balents, Nat. Phys. **6**, 376 (2010).
[4] J. Chaloupka, G. Jackeli, and G. Khaliullin, Phys. Rev. Lett. **105**, 027204 (2010).
[5] X. Wan, A. M. Turner, A. Vishwanath, and S. Y. Savrasov, Phys. Rev. B **83**, 205101 (2011).
[6] W. Witczak-Krempa, G. Chen, Y. B. Kim, and L. Balents, Annu. Rev. Condens. Matter Phys. **5**, 57 (2014).
[7] Z. Nussinov and J. v. d. Brink, arXiv:1303.5922.
[8] D. Yanagishima and Y. Maeno, J. Phys. Soc. Jpn. **70**, 2880 (2001).
[9] S. Nakatsuji, Y. Machida, Y. Maeno, T. Tayama, T. Sakakibara, J. van Duijn, L. Balicas, J. N. Millican, R. T. Macaluso, and J. Y. Chan, Phys. Rev. Lett. **96**, 087204 (2006).
[10] K. Matsuhira, M. Wakeshima, R. Nakanishi, T. Yamada, A. Nakamura, W. Kawano, S. Takagi, and Y. Hinatsu, J. Phys. Soc. Jpn. **76**, 043706 (2007).
[11] B. Kim, H. Jin, S. Moon, J.-Y. Kim, B.-G. Park, C. Leem, J. Yu, T. Noh, C. Kim, S.-J. Oh *et al.*, Phys. Rev. Lett. **101**, 076402 (2008).
[12] B. J. Kim, H. Ohsumi, T. Komesu, S. Sakai, T. Morita, H. Takagi, and T. Arima, Science **323**, 1329 (2009).
[13] Y. Singh and P. Gegenwart, Phys. Rev. B **82**, 064412 (2010).
[14] X. Liu, T. Berlijn, W.-G. Yin, W. Ku, A. Tsvelik, Y.-J. Kim, H. Gretarsson, Y. Singh, P. Gegenwart, and J. P. Hill, Phys. Rev. B **83**, 220403 (2011).
[15] S. K. Choi, R. Coldea, A. N. Kolmogorov, T. Lancaster, I. I. Mazin, S. J. Blundell, P. G. Radaelli, Y. Singh, P. Gegenwart, K. R. Choi, S.-W. Cheong, P. J. Baker, C. Stock, and J. Taylor, Phys. Rev. Lett. **108**, 127204 (2012).
[16] T. Qi, O. Korneta, X. Wan, L. DeLong, P. Schlottmann, and G. Cao, J. Phys.: Condens. Matter **24**, 345601 (2012).
[17] T. Takayama, A. Kato, R. Dinnebier, J. Nuss, and H. Takagi, arXiv:1403.3296.
[18] S. Mandal and N. Surendran, Phys. Rev. B **79**, 024426 (2009).
[19] Eric Kin-Ho Lee, R. Schaffer, S. Bhattacharjee, and Y. B. Kim, Phys. Rev. B **89**, 045117 (2014).
[20] S. B. Lee, Eric Kin-Ho Lee, A. Paramekanti, and Y. B. Kim, Phys. Rev. B **89**, 014424 (2014).
[21] I. Kimchi, J. G. Analytis, and A. Vishwanath, arXiv:1309.1171.
[22] A. Shitade, H. Katsura, J. Kuneš, X.-L. Qi, S.-C. Zhang, and N. Nagaosa, Phys. Rev. Lett. **102**, 256403 (2009).
[23] W. Witczak-Krempa and Y. B. Kim, Phys. Rev. B **85**, 045124 (2012).
[24] W. Urland and R. Hoppe, Z. Anorg. Allg. Chem. **392**, 23 (1972).

[25] L. Fu, C. L. Kane, and E. J. Mele, Phys. Rev. Lett. **98**, 106803 (2007).
[26] Eric Kin-Ho Lee, S. Bhattacharjee, and Y. B. Kim, Phys. Rev. B **87**, 214416 (2013).
[27] C. L. Kane and E. J. Mele, Phys. Rev. Lett. **95**, 226801 (2005).
[28] J. C. Slater and G. F. Koster, Phys. Rev. **94**, 1498 (1954).
[29] J. B. Goodenough, Phys. Rev. **171**, 466 (1968).
[30] S. Boker, M. Neale, H. Maes, M. Wilde, M. Spiegel, T. Brick, J. Spies, R. Estabrook, S. Kenny, T. Bates *et al.*, Psychometrika **76**, 306 (2011).
[31] J. P. Perdew, K. Burke, and M. Ernzerhof, Phys. Rev. Lett. **77**, 3865 (1996).
[32] T. Micklitz and M. R. Norman, Phys. Rev. B **81**, 174417 (2010).
[33] H.-S. Kim and H. Jin (unpublished).
[34] R. S. K. Mong, A. M. Essin, and J. E. Moore, Phys. Rev. B **81**, 245209 (2010).
[35] C. Fang, M. J. Gilbert, and B. A. Bernevig, Phys. Rev. B **88**, 085406 (2013).
[36] C.-X. Liu, arXiv:1304.6455.
[37] R.-X. Zhang and C.-X. Liu, arXiv:1401.6922.
[38] M. Hermanns and S. Trebst, arXiv:1401.7678.
[39] J. Reuther, R. Thomale, and S. Trebst, Phys. Rev. B **84**, 100406 (2011).
[40] K. Foyevtsova, H. O. Jeschke, I. I. Mazin, D. I. Khomskii, and R. Valentí, Phys. Rev. B **88**, 035107 (2013).
[41] J. G. Rau, Eric Kin-Ho Lee, and H.-Y. Kee, Phys. Rev. Lett. **112**, 077204 (2014).
[42] H. Gretarsson, J. Clancy, X. Liu, J. Hill, E. Bozin, Y. Singh, S. Manni, P. Gegenwart, J. Kim, A. Said *et al.*, Phys. Rev. Lett. **110**, 076402 (2013).
[43] C. Sohn, H.-S. Kim, T. Qi, D. Jeong, H. Park, H. Yoo, H. Kim, J.-Y. Kim, T. Kang, D.-Y. Cho *et al.*, Phys. Rev. B **88**, 085125 (2013).